1 Tree-ring cellulose oxygen isotope reveals summer

2 hydroclimate variability across the East European Plain

3

4 Qiaoyun Lin[1,2], Chenxi Xu[1,2,*], Ru Huang[1,3], Wenling An[1,*], Vladimir Matskovsky[4],

5 Olga Solomina[4,5], Ekaterina Dolgova[4], Yaru Zhao[1], Zhengtan Guo[1,2]

6

7 [1] State Key Laboratory of Lithospheric and Environmental Coevolution, Institute of Geology and
8 Geophysics, Chinese Academy of Sciences, Beijing 100029, China
9 [2] College of Earth and Planetary Sciences, University of Chinese Academy of Sciences, Beijing 100049,
10 China
11 [3] Department of Environment and Biodiversity, University of Salzburg, Salzburg, 5020, Austria
12 [4] Institute of Geography RAS, Moscow, Russia
13 [5] HSE University, Moscow, Russia

14 *Correspondence to*: Chenxi Xu (cxxu@mail.iggcas.ac.cn); Wenling An (wlan@mail.iggcas.ac.cn)

Abstract. Hydroclimate variability across the East European Plain plays a critical role in regional

ecosystems and climate dynamics, yet moisture-sensitive tree-ring proxies remain scarce in this region,

particularly at high latitudes where tree-ring width (TRW) and density are primarily controlled by

temperature. Tree-ring cellulose oxygen isotopes ($\delta^{18}O_{TRC}$) have the potential to serve as a useful

hydroclimate proxy, but their climatic signal in this region remain poorly understood. Here, we developed

three $\delta^{18}O_{TRC}$ chronologies of Scots pine (*Pinus sylvestris* L.) from the northern, central, and southern

East European Plain to assess their climate signals. The $\delta^{18}O_{TRC}$ chronologies from the three sites show

similar response to summer moisture condition. The northern $\delta^{18}O_{TRC}$ shows the strongest relationship

with vapor pressure deficit (VPD), the central $\delta^{18}O_{TRC}$ records both hydroclimate variability and

precipitation oxygen isotopes ($\delta^{18}O_p$) signals, and the southern $\delta^{18}O_{TRC}$ mainly reflects the Standardized

Precipitation Evapotranspiration Index (SPEI). In contrast, TRW shows weak hydroclimate sensitivity at

the northern and central sites, whereas at the southern site it mainly reflects soil moisture. Overall,

compared with TRW, $\delta^{18}O_{TRC}$ better captures regional summer hydroclimate signals, particularly

capturing signals related to atmospheric drought.

Keywords: East European Plain, *Pinus sylvestris* L., Tree-ring cellulose oxygen isotopes, Hydroclimate

1 Introduction

East European Plain occupies a pivotal position in the Eurasian climate system, serving as a key

transitional region between the North Atlantic, Europe, and the continental interior of Asia (Liu et al.,

2014; Morozova et al., 2023). Understanding climate variability in this region is fundamental for

interpreting large-scale climate variability across Eurasia. With global warming, this region has

experienced pronounced temperature increases accompanied by complex and spatially heterogeneous

changes in hydroclimate (Moberg et al., 2006; Spinoni et al., 2015; Zolina et al., 2009). Historical

analyses of hydroclimate variability over past centuries using proxy data are an essential quantitative

way to put current conditions in a longer-term perspective.

Tree-ring proxies have been widely used to reconstruct past climate because they are broadly

distributed, long-lived, annually resolved, and climate-sensitive (McCarroll and Loader, 2004). To date,

43 tree-ring width (TRW)-based climate-signal studies in the East European Plain span from the Arctic

44 margin to the southern Caucasus (Solomina and Matskovsky, 2021). However, the application of TRW

45 to climate reconstructions in this region remains limited. First, over the East European Plain, TRW–

46 climate relationships exhibit a boundary around 55–60° N: TRW is more temperature-limited to the north,

47 whereas it is more moisture-sensitive to the south (Matskovsky, 2016; Solomina and Matskovsky, 2021).

48 Second, TRW at most sites shows low-to-moderate climate sensitivity (correlation coefficients rarely

49 exceed 0.5) (Hughes et al., 2019; Solomina and Matskovsky, 2021). Consequently, although TRW has

50 been used to reconstruct past hydroclimate variability, moisture-sensitive sites capable of capturing

51 interannual hydroclimate variability remain scarce and unevenly distributed, particularly at high latitudes

52 (Cook et al., 2020; Kuznetsova and Solomina, 2022; Matskovsky et al., 2017). This motivates us to

53 explore alternative hydroclimate proxies with more directly process-based interpretations and stronger

54 moisture sensitivity.

55   Compared with TRW, tree-ring cellulose oxygen isotope ($\delta^{18}O_{TRC}$) typically shows lower within-

56 tree variability, higher inter-tree coherence, and no or very limited age-related effects, making it a widely

57 utilized hydroclimate proxy over the globe (Rinne, 2012; Römer et al., 2025; Xu et al., 2011). $\delta^{18}O_{TRC}$ is

58 mainly controlled by (i) the isotopic composition of source water ($\delta^{18}O_s$), which largely reflects

59 precipitation oxygen isotopes ($\delta^{18}O_p$), (ii) evaporative enrichment of leaf water, and (iii) oxygen

60 exchange with xylem water during cellulose formation (McCarroll and Loader, 2004; Roden et al., 2000).

61 These processes are modulated by factors such as temperature, precipitation amount, moisture-transport

62 history, relative humidity (RH), and wind speed (Gat, 1996; Roden et al., 2000). Consequently, $\delta^{18}O_{TRC}$

63 can preserve climate information from seasonal to interannual timescales and can be used to reconstruct

64 multiple hydroclimate variables, including precipitation (Rinne, 2012; Xu et al., 2023), RH (Haupt et al.,

65 2011), vapor pressure deficit (VPD) (Nagavciuc et al., 2024; Treydte et al., 2024), and drought indices

66 (An et al., 2023; Arosio et al., 2025; Freund et al., 2023; Xu et al., 2013a).

67   Although networks of tree-ring $\delta^{18}O$ chronologies have been widely developed across Europe and

68 Asia and applied to hydroclimate reconstructions (Freund et al., 2023; Treydte et al., 2024; Xu et al.,

69 2024), the climate sensitivity of $\delta^{18}O_{TRC}$ shows pronounced regional variability. The dominant climatic

70 controls on $\delta^{18}O_{TRC}$, as well as the strength and seasonal window of its response, can shift with changes

71 in moisture sources, transport pathways, and local moisture conditions (Freund et al., 2023; Treydte et

72 al., 2007). This spatial heterogeneity highlights the need for region-specific studies of climate signals. In

73   contrast, tree-ring isotope research in the East European Plain is limited (Matskovsky et al., 2022;

74   Panyushkina et al., 2016), and the ability of $\delta^{18}O_{TRC}$ to capture interannual hydroclimate variability in

75   this region remains a significant knowledge gap.

76   Given the pronounced north–south gradients and spatial heterogeneity in interannual variability and

77   long-term trends of temperature and precipitation (Klimenko and Solomina, 2010), a single site cannot

78   adequately represent the regional-scale climate sensitivity of $\delta^{18}O_{TRC}$. Here, we sampled Scots pine

79   (*Pinus sylvestris* L.) from three representative forest regions in the northern, central, and southern East

80   European Plain (51–65° N) and developed site-level $\delta^{18}O_{TRC}$ chronologies along this transect. Our

81   objectives were to (1) quantify the relative contributions of $\delta^{18}O_p$ and RH-related evaporative enrichment

82   to the spatial difference in $\delta^{18}O_{TRC}$; (2) identify the dominant climate signal and key seasonal windows

83   of $\delta^{18}O_{TRC}$ at the interannual scale; and (3) evaluate the potential of $\delta^{18}O_{TRC}$ for reconstructing historical

84   hydroclimate variability in the East European Plain.

85   **2 Material and methods**

86   **2.1 Study area**

87   The study area is located in the East European Plain and is characterized by cold winters, warm

88   summers, and pronounced seasonality. The relatively flat topography of the East European Plain, together

89   with the low relief of Central and Western Europe, allows Atlantic moisture carried by the prevailing

90   westerlies to penetrate far inland toward the Ural Mountains (Klimenko and Solomina, 2010).

91   The geographic locations of the three sampling sites are shown in Fig. 1a and Table 1. The northern

92   sampling site is located on the Solovetsky Islands, which have a subarctic climate. Owing to the maritime

93   influence of the White Sea, the islands experience milder temperatures, smaller diurnal temperature

94   ranges, higher humidity, and stronger winds than the adjacent mainland coast (Semenyak and Dolgova,

95   2023). The central sampling site is located in Yaroslavl city and has a temperate continental climate. The

96   surrounding forests are mainly coniferous and dominated by Scots pine. The site lies within a forest park

97   in an urban zone and may be influenced by anthropogenic disturbance. The southern sampling site is

98   located in Khrenovskoy Forest (Voronezh Oblast) and has a temperate continental climate. The forest

99   lies in the forest-steppe zone and represents the southernmost natural pine forest in the East European

100   Plain (Matskovsky et al., 2017), with Scots pine as the dominant tree species (Matveev et al., 2017).

101   From 1950–2021 (precipitation for the central site is only available for 1967–2021; Fig. 1b–d),

102   mean annual precipitation was 480, 623, and 489 mm at the northern, central, and southern sites,

103   respectively. Mean annual temperatures were 1.52, 3.85, and 6.51 °C, respectively. Summer (June–

104   August) mean temperatures decreased from 19.66 °C in the south to 16.73 °C in the central region, with

105   the lowest values in the north (12.86 °C). The lowest mean RH occurred in June at the northern site

106   (69.54 %) and in May at the central (63.56 %) and southern (56.71 %) sites (Fig. 1b–d).

107   Scots pine was selected as the study species. It is long-lived (up to ~400 years) and widely

108   distributed across northern Eurasia (Lange et al., 2018). Xylogenesis observations indicate pronounced

109   latitudinal differences in growth phenology: in northern insular ecosystems near our northern site, growth

110   typically begins in early June and ceases by mid to late August, whereas at more southerly sites xylem

111   formation generally starts earlier (from late April to May) and ends later (from late August to September)

112   (Matulewski et al., 2019; Matveev et al., 2020; Tishin et al., 2016).
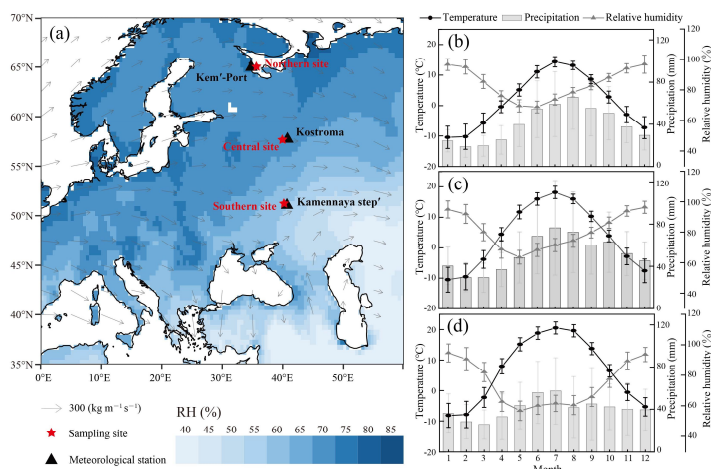
113

114   Figure 1. Study site locations and climatic characteristics. (a) Arrows indicate the mean vertically integrated water

115   vapor flux (kg m^{-1} s^{-1}) and the transport direction for May to September, 1950–2019. (b–d) show mean monthly

116   temperature, precipitation, and RH at the northern, central, and southern sites, respectively. Temperature and

117   precipitation data were obtained from meteorological stations, whereas RH was calculated from CRU TS 4.08

118   gridded temperature and vapor pressure (Harris et al., 2020). All mean monthly values are for 1950–2021, except

119   for central-site precipitation (1967–2021).

120

121   Table 1. Location, environmental characteristics, and $\delta^{18}O_{TRC}$ chronology statistics.

Site	Latitude (° N)	Longitude (° E)	Elevation (m)	Mean $\delta^{18}O_{TRC}$ (‰)	SD (‰)	AC1	Rbar	EPS	Age (yr)
N	65.039	35.641	9m	26.36	0.60	−0.09	0.67	0.89	1950–2021
C	57.647	39.932	110m	27.61	0.61	0.15	0.57	0.84	1950–2020
S	51.201	40.199	94m	30.52	0.68	0.13	0.58	0.84	1950–2014

122 N, C, S denote northern, central, southern sites, respectively. SD, AC1, Rbar, and EPS represent the standard

123 deviation, first-order autocorrelation, mean interseries correlation, and expressed population signal, respectively.

124 **2.2 Sampling, Sample Preparation and Isotope Analysis**

125 Initially, the cores were collected for dendroclimatic analysis at breast height using increment corers

126 from dominant and subdominant trees. The cores were mounted on wooden bases with polyvinyl alcohol

127 (PVA) glue, polished, and scanned. Tree-ring widths (TRW) were measured in CooRecorder, and cross-

128 dating was verified for all samples using COFECHA (Holmes, 1983). The TRW chronologies used in

129 this study were developed by detrending and standardizing the ring-width series with the ARSTAN

130 program. Previous analyses of TRW data from these sites are available in Dolgova et al. (2022) and

131 Semenyak and Dolgova (2023). For $\delta^{18}O_{TRC}$ analysis, we selected four crossdated cores from four

132 individual trees without missing rings or extremely narrow rings for each site. Given better sample

133 availability at the northern site, we increased the number of tree cores from 4 to 7 and extended the

134 isotope series from 2016 to 2021.

135 α-cellulose was extracted using a modified plate method (Xu et al., 2011, 2013b). Cores were cut

136 into ~1 mm thick, and ~7 cm long slivers and processed following the Jayme–Wise protocol (Loader et

137 al., 1997). Specifically, lignin, hemicellulose, and lipids were sequentially removed by treatment with

138 acidified $NaClO_2$, 17 wt% NaOH, and organic solvents (acetone, toluene, and ethanol), respectively.

139 After chemical treatment, the α-cellulose slivers were oven-dried at 70 °C. Annual α-cellulose

140 subsamples were separated under a binocular microscope using a scalpel. The α-cellulose samples (0.12–

141 0.20 mg) were weighed and wrapped in silver foil for oxygen isotope analysis.

142 $\delta^{18}O_{TRC}$ values were measured at the Institute of Geology and Geophysics, Chinese Academy of

143 Sciences, using an isotope ratio mass spectrometer (Delta V Advantage, Thermo Scientific, Germany)

144 coupled to a high-temperature conversion elemental analyzer (Flash HT, Thermo Scientific, Germany).

145 Oxygen isotope ratios are reported in δ notation relative to Vienna Standard Mean Ocean Water

146 (VSMOW): $\delta^{18}O = [(R_{sample}/R_{standard}) - 1] \times 1000‰$, where R_{sample} and $R_{standard}$ denote the $^{18}O/^{16}O$ ratios

147 of the sample and standard, respectively. For calibration and quality control, a Merck cellulose working

148 standard was analyzed after every eight samples, and $\delta^{18}O$ values were normalized to this standard. The

149 analytical uncertainties for repeated measurements of Merck cellulose were $\sim \pm 0.16‰$ (n = 149).

150 **2.3 Climate data**

151 Temperature and precipitation data for the northern, central, and southern sites were obtained from

152 the Kem'-Port Meteorological Station (34.80° E, 64.98° N; WMO No. 22520), Kostroma Meteorological

153 Station (40.78° E, 57.73° N; WMO No. 27333), and Kamennaya Step' Meteorological Station (40.70° E,

154 51.05° N; WMO No. 34139), respectively (Fig. 1a). All meteorological station data were obtained from

155 the Russian Institute of Hydrometeorological Information-World Data Centre (RIHMI-WDC).

156 To examine contemporaneous and lagged relationships between $\delta^{18}O_{TRC}$ and additional climatic

157 variables, we used gridded products from the following archives. These included monthly mean

158 temperature (T_{mean}), maximum temperature (T_{max}), minimum temperature (T_{min}), precipitation (Pre),

159 cloud cover (CC), and vapor pressure (VP) from CRU TS 4.08 at 0.5° × 0.5° spatial resolution for 1950–

160 2021 (Harris et al., 2020); drought indices including the Standardized Precipitation Evapotranspiration

161 Index (SPEI) and the Palmer Drought Severity Index (PDSI)(Dai et al., 2004; Vicente-Serrano et al.,

162 2010b); and soil moisture (SM; 0–10 cm and 0–40 cm) from the Famine Early Warning Systems Network

163 Land Data Assimilation System (FLDAS) at 0.1° × 0.1° resolution (McNally et al., 2017).

164 All gridded datasets were accessed and downloaded via the KNMI Climate Explorer (Trouet and

165 Van Oldenborgh, 2013). For each site, gridded variables were spatially averaged within a 2° × 2° box

166 centered on the sampling coordinates. Monthly T_{mean} and VP were used to calculate RH and VPD

167 following formulae (Allen et al., 1998):

168 $$RH=(VP/e_{sat})\times100 \tag{1}$$

169 $$e_{sat}=6.108\times\exp(17.27\times T/(T+237.3)) \tag{2}$$

170 $$VPD=e_{sat}\text{-}VP \tag{3}$$

171 where e_{sat} is saturated vapor pressure (hPa), and T is mean temperature (°C).

172 Given that $\delta^{18}O_p$ is an important control on $\delta^{18}O_{TRC}$, and that nearby Global Network of Isotopes in

173 Precipitation (GNIP; https://www.iaea.org/zh/fu-wu/wang-luo) records are relatively short, GNIP

174 observations alone are insufficient for long-term analyses. Therefore, we used the isotope-enabled

175   atmospheric general circulation model ECHAM5-wiso to obtain $\delta^{18}O_P$ for our study region. ECHAM5-

176   wiso is an isotope-enabled extension of ECHAM5 in which the stable water isotopologues $H_2^{18}O$ and

177   HDO are explicitly simulated within the atmospheric hydrological cycle (Werner et al., 2011). We

178   downloaded model-simulated monthly $\delta^{18}O_P$ (https://doi.pangaea.de/10.1594/PANGAEA.902347) and

179   extracted time series from the grid cell nearest to each study site for 1958–2013. Previous studies have

180   evaluated ECHAM5-wiso against GNIP observations at the global scale (Werner et al., 2011) and across

181   Europe (Langebroek et al., 2011). Moreover, ECHAM5-wiso successfully reproduced the seasonal

182   phase of $\delta^{18}O_P$ observed at nearby GNIP stations, despite a pronounced station-dependent mean offset,

183   particularly at southern stations with limited GNIP coverage (Fig. S1). Consequently, we primarily used

184   ECHAM5-wiso $\delta^{18}O_P$ simulations to interpret interannual variability in source-water isotopes. The

185   latitude, longitude, and other metadata for the simulated and observed $\delta^{18}O_P$ data are provided in Table

186   S1.

187   **2.4 Statistical analyses**

188   The $\delta^{18}O_{TRC}$ series from all analyzed cores at each site were averaged to generate site-level $\delta^{18}O_{TRC}$

189   chronologies for the northern, central, and southern sites. We calculated the mean interseries correlation

190   (Rbar) to evaluate inter-core coherence and the expressed population signal (EPS) to assess chronology

191   representativeness (Wigley et al., 1984). To explore the factors controlling the spatial differences in

192     $\delta^{18}O_{TRC}$, we used a simplified mechanistic fractionation framework for $\delta^{18}O_{TRC}$ (Roden et al., 2000):

193                 $$\delta^{18}O_{TRC}=(\delta^{18}O_S+\varepsilon_0)+\alpha(1\text{-}f_0)(1\text{-}h)(\varepsilon^*+\varepsilon_k) \tag{4}$$

194   Here, $\delta^{18}O_S$ is the oxygen isotopic composition of source water (approximated by $\delta^{18}O_P$); ε_0 is the

195   net biochemical fractionation term associated with cellulose formation; f_0 is the proportion of

196   exchangeable oxygen during cellulose synthesis (set to 0.42; Sternberg and Ellsworth, 2011); ε^* and ε_k

197   are the equilibrium and kinetic fractionation factors, respectively (set to 9‰ and 29‰, respectively;

198   Allison et al., 1985); h is the relative humidity at the evaporative site in the leaf; and α is a

199   scaling/attenuation factor describing the transfer of the evaporative-enrichment signal to cellulose (set to

200   1; Allison et al., 1985; Barbour, 2007).

201   We further defined the evaporative enrichment term, E, as

202                 $$E=\alpha(1\text{-}f_0)(1\text{-}h)(\varepsilon^*+\varepsilon_k) \tag{5}$$

203   Here, Δ denotes the pairwise difference between sites. We then calculated $\Delta\delta^{18}O_{TRC}$, $\Delta\delta^{18}O_P$, ΔRH,

204 and ΔE to quantify the relative contributions of site-to-site differences in $\delta^{18}O_p$ and RH-controlled

205 evaporative enrichment to spatial variability in $\delta^{18}O_{TRC}$.

206   To identify climatic and source-water signals recorded in $\delta^{18}O_{TRC}$, we correlated the chronology

207 with monthly and seasonal climate variables from June of the previous year to September of the current

208 year, and with $\delta^{18}O_p$ from October of the previous year to September of the current year. Spatial

209 correlations between each site chronology and gridded CRU TS 4.08 data were calculated using the

210 KNMI Climate Explorer (https://climexp.knmi.nl/start.cgi) to evaluate the regional representativeness of

211 $\delta^{18}O_{TRC}$.

212 **3 Results**

213 **3.1 Tree-ring cellulose oxygen isotope chronologies**

214   The mean inter-series correlation (Rbar) for the northern $\delta^{18}O_{TRC}$ site was 0.67, and the expressed

215 population signal (EPS) of the chronology was 0.89 (Table 1). By contrast, the central and southern sites

216 showed slightly lower values (Rbar = 0.57 and 0.58, respectively; EPS = 0.84 for both sites; Table 1).

217 Along the north–south transect, the series were averaged to build $\delta^{18}O_{TRC}$ chronologies for the North

218 (1950–2021), Central (1950–2020), and South (1950–2014) (Fig. 2a–d). EPS was $\geqslant$ 0.84 at all three

219 sites, indicating that the chronologies effectively capture a common environmental signal. The high

220 within-site inter-series correlations (Table S2) further support the reliability of the $\delta^{18}O_{TRC}$ chronologies.

221   The northern $\delta^{18}O_{TRC}$ chronology ranged from 24.85‰ to 27.99‰, with a mean of 26.36‰, a

222 standard deviation (SD) of 0.60‰, and a first-order autocorrelation (AC1) of −0.09 (Table 1). The central

223 chronology ranged from 26.23‰ to 28.76‰, with a mean of 27.61‰, an SD of 0.61‰, and an AC1 of

224 0.15 (Table 1). The southern chronology ranged from 28.93‰ to 31.79‰, with a mean of 30.52‰, an

225 SD of 0.68‰, and an AC1 of 0.13 (Table 1). Over the common period (1950–2014), the northernmost

226 Solovetsky Islands chronology had the lowest median (26.35‰), the central site was 27.62‰, and the

227 southernmost site had the highest median (30.54‰) (Fig. 2e). Overall, both the mean and median values

228 of the East European Plain $\delta^{18}O_{TRC}$ chronologies show a clear latitudinal gradient, with higher values in

229 the south and lower values in the north.

230   Pairwise correlations among the three chronologies ranged from 0.14 to 0.35 over 1950–2014.

231 Significant correlations were found for the North–Central pair (NC; r = 0.33, $p < 0.01$) and the Central–

232 South pair (CS; r = 0.35, $p < 0.01$), whereas the North–South pair (NS; r = 0.14, $p > 0.05$) was not

233 significant (Fig. 2e). Overall, these results suggest that $\delta^{18}O_{TRC}$ variability shows local coherence, with

234 stronger similarity between adjacent sites that weakens with increasing distance.
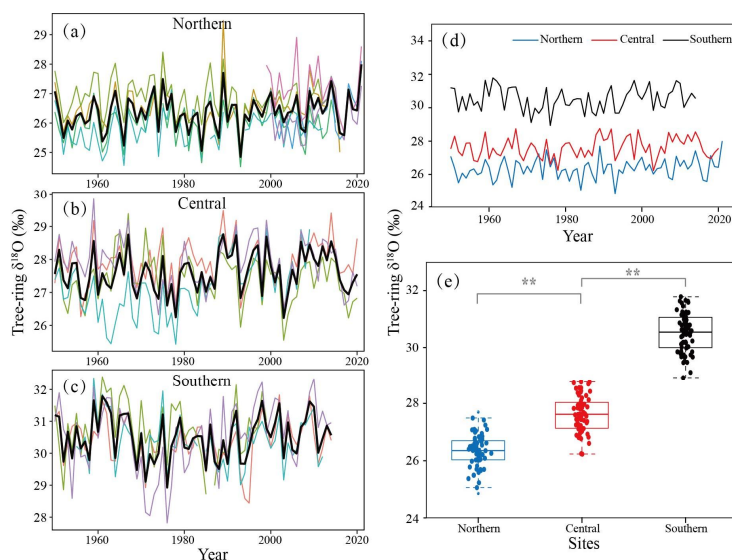
235

236 Figure 2. $\delta^{18}O_{TRC}$ chronologies for the northern (a), central (b), and southern (c) East European Plain. Individual

237 $\delta^{18}O_{TRC}$ series are shown as thin colored lines; the site mean chronology is shown as thick black lines. Time-series

238 plots (d) and box-and-whisker plots (e; 1950–2014) show the $\delta^{18}O_{TRC}$ chronologies at the three sites. In panel (e),

239 the line within each box denotes the median; box limits indicate the 25th and 75th percentiles; and filled circles

240 denote outliers. Asterisks indicate statistical significance (**, $p < 0.01$).

241 **3.2 Climate responses and source water signals of $\delta^{18}O_{TRC}$**

242 During the growing season or summer, $\delta^{18}O_{TRC}$ is significantly positively correlated with VPD, but

243 significantly negatively correlated with moisture-related variables such as Pre, RH, CC, SPEI, PDSI, and

244 SM (Fig. 3; Table S3–S5). Among the three sites, the northern site shows the strongest atmospheric

245 drying signal, with the highest correlation between $\delta^{18}O_{TRC}$ and May–September VPD (r = 0.61, $p < 0.01$,

246 n = 72) (Fig. 3; Table S3). In contrast, moisture signals are weaker at the central and southern sites:

247 $\delta^{18}O_{TRC}$ at central site correlates with May–September SPEI at r = −0.42 ($p < 0.01$, n = 69), whereas the

248 strongest relationship at the southern site is with June–August SPEI (r = −0.51, $p < 0.01$, n = 65) (Fig. 3;

249 Table S4–S5). By comparison, moisture conditions in the previous year and in spring (March–May) exert

250 relatively limited influence on $\delta^{18}O_{TRC}$, with only a few variables showing significant effects in isolated

251   months.

252   Overall, correlation analyses between $\delta^{18}O_{TRC}$ and local climate factors indicate that all three sites

253   consistently capture hydroclimatic variability. Results based on first-differenced chronologies further

254   support these patterns (Fig. S2). Correlation strengths at the northern site changed little after differencing,

255   whereas correlations with moisture-related indices become stronger at the central and southern sites,

256   indicating that the interannual correspondence between $\delta^{18}O_{TRC}$ and hydroclimate becomes clearer once

257   low-frequency variability is reduced (Fig. S2).

258   In addition to the moisture signal, $\delta^{18}O_{TRC}$ at all three sites also exhibits significant temperature

259   responses. The central site shows the strongest summer temperature signal, with $\delta^{18}O_{TRC}$ correlated with

260   June–September T_{max} ($r = 0.45$, $p < 0.01$, $n = 71$) (Fig. 3), and this relationship remains nearly unchanged

261   when using first-differenced series (Fig. S2). Notably, the temperature influence is not confined to

262   summer, but extends into the previous cold season and the current spring. Further analyses show stronger

263   correlations between $\delta^{18}O_{TRC}$ and broader seasonal temperature windows: the northern site correlates

264   with March–September T_{max} ($r = 0.50$), while the central and southern sites correlate with mean

265   temperature from the previous October to the current September (both $r = 0.48$), exceeding the strength

266   of summer-only temperature signals.
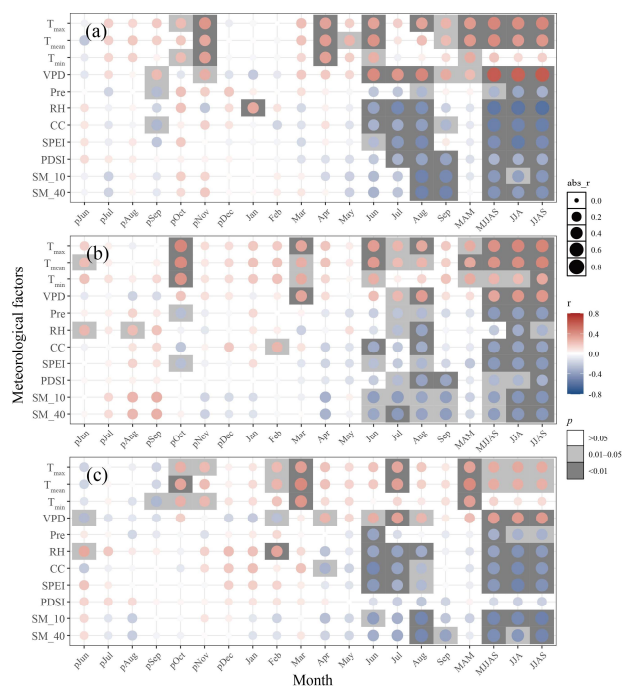
267

268   Figure 3. Correlations between $\delta^{18}O_{TRC}$ and meteorological factors for the northern (a), central (b), and southern (c)

269   sites in the East European Plain. The time periods are 1950–2021 (north), 1950–2020 (central), and 1950–2014

270   (south), except for SPEI (1950–2018) at the northern and central sites and SM (1982 to the end year of each

271   chronology) at all sites. T_{mean} and precipitation were obtained from meteorological stations, except that precipitation

272   at the central site was taken from the CRU TS 4.08 dataset.

273   Source-water signals in the three $\delta^{18}O_{TRC}$ chronologies are shown in Fig. 4. At all sites, $\delta^{18}O_{TRC}$

274   showed its strongest correlations with $\delta^{18}O_p$ in early summer (June–July), with r = 0.47, 0.68, and 0.42

275   from north to south ($p < 0.01$; Fig. 4). Following first-order differencing, these correlations changed only

276   slightly (Fig. S3). At the northern site, $\delta^{18}O_{TRC}$ was also positively correlated with $\delta^{18}O_p$ in January and

277   March of the current year. At the central site, $\delta^{18}O_p$ in the previous September, October, and December,

278   as well as in January and May of the current year, was positively associated with $\delta^{18}O_{TRC}$. In contrast, at

279   the southern site, $\delta^{18}O_p$ outside June–July showed no significant relationship with $\delta^{18}O_{TRC}$.
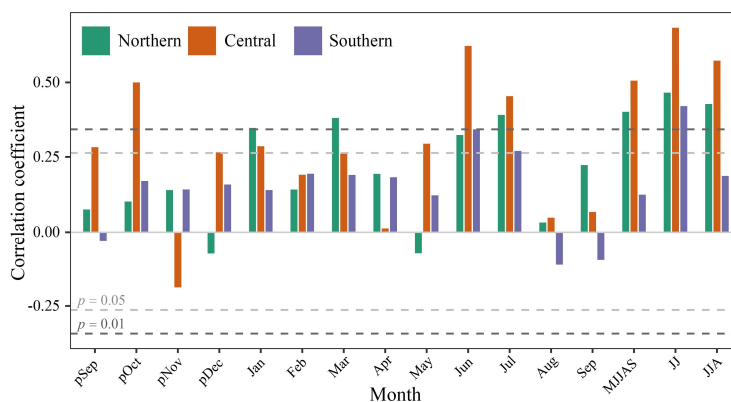
281   Figure 4. Correlations between $\delta^{18}O_{TRC}$ and $\delta^{18}O_p$ (1958–2013).

282   For the spatial difference between the northern and central sites (NC), the $\delta^{18}O_{TRC}$ difference is

283   −1.288‰. In this case, $\Delta\delta^{18}O_p$ (−1.159‰) is larger than the difference in the enrichment term (−0.688‰),

284   indicating that source-water isotopic differences dominate the NC $\delta^{18}O_{TRC}$ spatial offset (Table 2). In

285   contrast, the $\delta^{18}O_{TRC}$ difference between the central and southern sites (CS) is −2.884‰, and the

286   enrichment-term difference (−2.242‰) exceeds $\Delta\delta^{18}O_p$ (−1.295‰). Together with the larger RH

287   difference (ΔRH = 10.174%), this suggests that stronger evaporative enrichment is the primary driver of

288   the $\delta^{18}O_{TRC}$ offset between the Central and Southern sites (Table 2). The overall difference between the

289     $\delta^{18}O_{TRC}$ from northern and southern sites (NS) is −4.172‰, with comparable magnitudes for $\Delta\delta^{18}O_p$

290   (−2.454‰) and the enrichment term (−2.930‰) (Table 2). Estimates based on observed $\delta^{18}O_p$ also

291   support this pattern, showing a consistent north–south gradient (Table S6).

292

293   Table 2. Pairwise differences (Δ) in $\delta^{18}O_{TRC}$, modeled $\delta^{18}O_P$, RH, and the RH-driven enrichment term (May–

294   September mean, 1958–2013; NC = North−Central, CS = Central−Southern, NS = North−Southern).

Pair	$\Delta\delta^{18}O_{TRC}$	$\Delta\delta^{18}O_P$	ΔRH	ΔE
NC	−1.288	−1.159	3.121	−0.688
CS	−2.884	−1.295	10.174	−2.242
NS	−4.172	−2.454	13.295	−2.930

295   **3.3 Spatial correlations of $\delta^{18}O_{TRC}$ with hydroclimate and $\delta^{18}O_P$**

296   Spatial correlation analyses based on gridded hydroclimate metrics (SPEI, VPD, and RH) indicate

297   that $\delta^{18}O_{TRC}$ at all three sites exhibited a consistent response to regional summer moisture conditions: it

298   shows significant positive correlations with June–August VPD over broad areas, but significant negative

299   correlations with RH and SPEI (Fig. 5). At the northern site, the strongest correlations formed a spatially

300   coherent significant region over the White Sea area and adjacent northern Europe (Fig. 5a, d, g). The

301   central site showed a similar but weaker pattern, with significant regions mainly covering the central East

302   European Plain and extending eastward (Fig. 5b, e, h). At the southern site, significant regions were

303   primarily distributed over the southern East European Plain (Fig. 5c, f, i). In addition, spatial correlations

304   with ECHAM5-wiso–simulated $\delta^{18}O_P$ further suggested a coherent source-water isotopic imprint in

305    $\delta^{18}O_{TRC}$ (Fig. S4). Overall, $\delta^{18}O_{TRC}$ reflected both regional summer hydroclimate and $\delta^{18}O_P$ variability,

306   with broadly consistent spatial patterns across sites but differing strengths.
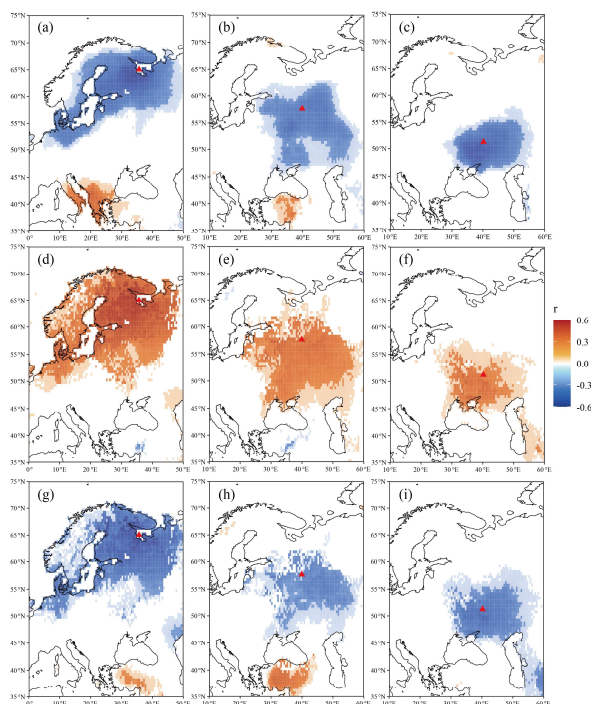
Figure 5. Spatial correlations between $\delta^{18}O_{TRC}$ and summer (June–August) hydroclimate variables: SPEI (a–c), VPD (d–f), and RH (g–i). Columns correspond to the northern (a, d, g), central (b, e, h), and southern (c, f, i) sites in the East European Plain; the corresponding year ranges are provided in the figure legend for Fig. 3.

3.4 Climate responses of tree-ring width

The climatic sensitivity of TRW differs markedly among the three sites (Fig. 6). Because the SM record is relatively short, we do not use it as the primary basis for identifying dominant controls, although its correlations are significant. TRW at the northern and southern sites shows significant summer hydroclimate sensitivity, with the strongest relationships in both cases occurring for PDSI (north: July, r = 0.36; south: June–September, r = 0.54; Fig. 6a, c). By contrast, TRW at the central site shows little evidence of a stable moisture response (Fig. 6b). TRW at all three sites is also significantly sensitive to temperature, but the optimal response window shifts earlier toward lower latitudes: the northern site responds mainly to midsummer (July–August) temperature, the central site to early spring (March–April), and the southern site to late winter–early spring (January–March) (Fig. 6). Overall, the climatic responses of TRW exhibit clear regional differentiation: temperature and moisture signals are of comparable

14

322   strength at the northern site, the central site is dominated by temperature, and the southern site is primarily

323   controlled by moisture conditions.
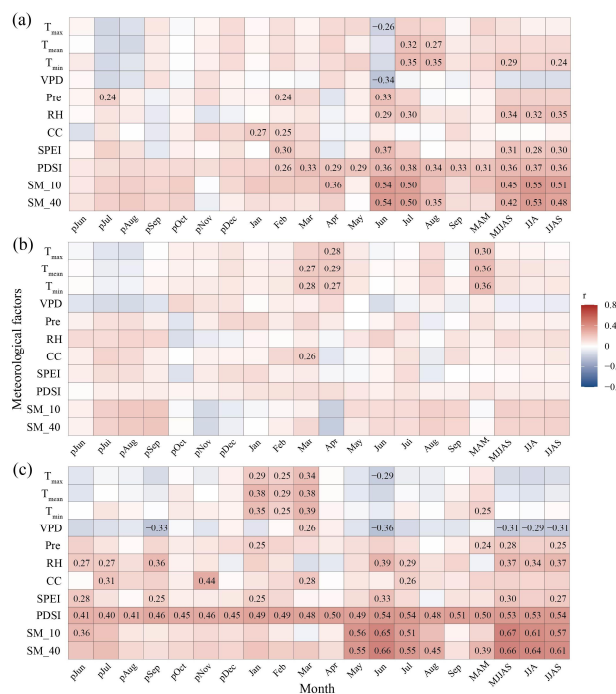
324

325   Figure 6. Correlations between TRW and meteorological factors for the northern (a), central (b), and southern (c)

326   sites in the East European Plain. Time periods and meteorological data sources are the same as in Fig. 3, except

327   that the northern TRW chronology spans 1950–2016. Numbers shown in the figure indicate correlations significant

328   at $p < 0.05$.

329   **4 Discussion**

330   **4.1 Spatial latitudinal gradient of $\delta^{18}O_{TRC}$ across the East European Plain**

331         $\delta^{18}O_P$ and RH-regulated leaf-water evaporative enrichment jointly control spatial variations in

332    $\delta^{18}O_{TRC}$ (Roden et al., 2000). Across the East European Plain, $\delta^{18}O_P$ shows higher values in the south than

333   in the northern region (Fig. S5), whereas regional RH exhibits a wetter north–drier south gradient (Fig.

334   1). These large-scale gradients are broadly consistent with the southward increase in $\delta^{18}O_{TRC}$ across the

335   region (Table 1; Fig. 2). Further analyses indicate that the dominant controlling factors on the spatial

336   variability of $\delta^{18}O_{TRC}$ are different between the NC and CS site pairs.

15

337   For the NC pair, the between-site difference in $\delta^{18}O_p$ is clearly larger than the corresponding

338   difference in RH-driven evaporative enrichment (Table 2), indicating that $\delta^{18}O_p$ is the primary driver.

339   This pattern is expected because $\delta^{18}O_{TRC}$ partly reflects the isotopic composition of source water via soil-

340   water uptake and therefore often covaries positively with $\delta^{18}O_p$ (Saurer et al., 2000). In mid- to high-

341   latitude regions, the "amount effect" is generally weak, whereas temperature often exerts a dominant

342   control on $\delta^{18}O_p$ (Krklec et al., 2018; Rozanski et al., 1992). At higher latitudes, lower condensation

343   temperatures and stronger isotopic fractionation, together with progressive rainout during poleward

344   transport, deplete ^{18}O in the remaining vapor and result in lower $\delta^{18}O_p$ values (Dansgaard, 1953; Gat,

345   1996). Global observations support this mechanism, showing an average decrease of ~0.5‰ per 1°

346   increase in latitude (Rozanski et al., 1992). In addition, the RH difference between the northern and

347   central sites is relatively small (Fig. 1; Fig. S5), resulting in a relatively limited between-site contrast in

348   evaporative enrichment. Together, these mechanisms explain why source-water isotopes dominate spatial

349   difference in $\delta^{18}O_{TRC}$ between the NC sites.

350   For the CS pair, the RH contrast is much larger than that in the NC pair (Fig. 1; Fig. S5). Consistently,

351   the between-site difference in RH-driven evaporative enrichment exceeds the corresponding difference

352   in $\delta^{18}O_p$ (Table 2), indicating that drier southern conditions enhance evaporative enrichment and

353   contribute more to $\Delta\delta^{18}O_{TRC}$. Lower RH strengthens the leaf-to-atmosphere evaporative gradient,

354   increasing ^{18}O enrichment in leaf water and its transfer to cellulose   (Roden et al., 2000). A modeling

355   study further indicates that spatial variation in leaf-water evaporative enrichment is closely linked to

356   atmospheric humidity, with drier conditions favoring greater ^{18}O enrichment (Keel et al., 2016). Similar

357   humidity-driven patterns have been reported elsewhere, for example along a north–south gradient in the

358   tropical Andes, where $\delta^{18}O_{TRC}$ increases toward drier southern sites (Álvarez et al., 2024).

359   Comparable large-scale latitudinal patterns in $\delta^{18}O_{TRC}$ has also been documented in other regions,

360   including the European tree-ring $\delta^{18}O$ network (Balting et al., 2021), the Asian tree-ring $\delta^{18}O$ network

361   (Huang et al., 2025; Xu et al., 2021, 2024), and eastern Anatolia (Mutlu et al., 2012). Across Europe,

362   spatial variability in tree-ring $\delta^{18}O$ has been attributed to the combined effects of latitude, elevation, and

363   continentality (Balting et al., 2021; Mutlu et al., 2012). Across Asia, the tripolar pattern in tree-ring $\delta^{18}O$

364   primarily reflects the latitudinal structure of $\delta^{18}O_p$, with RH-controlled enrichment acting as a key

365   modulator, particularly in mid-latitudes (Huang et al., 2025; Xu et al., 2024). Similar to patterns reported

366   in Asian, spatial variability in the East European Plain reflects a dual control: the mid- to high-latitude

367   NC pair is dominated by $\delta^{18}O_P$, whereas the mid-latitude CS pair is driven primarily by RH-controlled

368   enrichment. Together, these mechanisms produce a south-to-north decrease in $\delta^{18}O_{TRC}$ across the region.

369   **4.2 Interannual climatic implications of $\delta^{18}O_{TRC}$ in the East European Plain**

370   Based on the mechanistic framework of cellulose $\delta^{18}O$, $\delta^{18}O_{TRC}$ integrates both $\delta^{18}O_P$ and

371   evaporative enrichment of leaf water (McCarroll and Loader, 2004; Roden et al., 2000). Across the three

372   sites, $\delta^{18}O_{TRC}$ records a coherent interannual signal during the growing season and summer: values tend

373   to increase under higher evaporative demand and more enriched $\delta^{18}O_P$, and decrease under more humid

374   conditions (Fig. 3; Fig. S2).

375   On the source-water side, interannual variability in source-water $\delta^{18}O$ is linked to temperature- and

376   precipitation-related processes (Dansgaard, 1964; Rozanski et al., 1992). Higher temperature and VPD

377   can enhance soil evaporation and enrich near-surface soil water, whereas higher precipitation and SM

378   tend to reduce evaporative enrichment and $\delta^{18}O_s$. In parallel, the strong linkages of $\delta^{18}O_{TRC}$ with moisture

379   indicate leaf-water evaporative enrichment as a key control (McCarroll and Loader, 2004; Roden et al.,

380   2000), because root uptake involves negligible isotopic fractionation (Dawson and Ehleringer, 1991).

381   Lower RH (higher VPD) enhances leaf-water ^{18}O enrichment and its transfer to cellulose (McCarroll and

382   Loader, 2004; Roden et al., 2000); CC likely reflects coupled radiative–humidity effects on enrichment

383   (Wang et al., 2022). Finally, SPEI and PDSI integrate precipitation supply and evaporative demand (Dai

384   et al., 2004; Vicente-Serrano et al., 2010b), which is consistent with their coherent relationships with

385    $\delta^{18}O_{TRC}$ as integrated indicators of hydroclimate (Xu et al., 2013a).

386   Despite the overall similarity in response patterns, the dominant controls on interannual $\delta^{18}O_{TRC}$

387   variability differ among sites. The central site exhibits both a pronounced source-water isotopic imprint

388   and a leaf-water enrichment signal (Fig. 3–4; Fig. S2). Significant correlations between $\delta^{18}O_{TRC}$ and

389    $\delta^{18}O_P$ in both the original and first-differenced series indicate that interannual anomalies in source-water

390    $\delta^{18}O$ are effectively transmitted into cellulose. Together with the relatively larger interannual variability

391   in $\delta^{18}O_P$ and smaller variability in RH (Fig. S5), this suggests that the source-water signal is more readily

392   expressed statistically. By contrast, correlations with humidity-related metrics become markedly stronger

393   after differencing, indicating that low-frequency variability partly obscures the interannual hydroclimate

394   signal (Fig. S2). The weaker humidity signal in the original series may reflect the urban forest-park

395   setting of the central site, where canopy buffering and local anthropogenic influences can decouple near-

396 canopy humidity from the broader gridded macroclimatic background at low frequencies (De Frenne et

397 al., 2019; Zellweger et al., 2020). In addition, the strong T_{max} response changes little after differencing,

398 implying that it is not solely trend-driven and may partly reflect temperature-related modulation of

399 regional $\delta^{18}O_p$ and associated processes (Field et al., 2022; Leland et al., 2023).

400   In contrast, humidity signals are more pronounced at the northern and southern sites, although the

401 underlying mechanisms differ. The northern $\delta^{18}O_{TRC}$ chronology shows a stable VPD signal (Fig. 4; Fig.

402 S2; Fig. S6). The Solovetsky Islands lie in a cold and moist high-latitude environment (Fig. 1), where

403 tree growth is more strongly temperature-limited. Under such conditions, warming tends to increase

404 atmospheric evaporative demand (Zharkov et al., 2021), allowing evaporative-demand–driven leaf-water

405 enrichment to exert a stable control on interannual $\delta^{18}O_{TRC}$ variability. Similarly, studies from high-

406 latitude northern Europe have reported clear summer VPD signals in $\delta^{18}O_{TRC}$ and have used $\delta^{18}O_{TRC}$

407 networks to reconstruct regional-scale VPD (Treydte et al., 2024). By comparison, the southern site is

408 characterized by a drier climatic background with lower RH (Fig. 1; Fig. S5), and $\delta^{18}O_{TRC}$ shows its

409 strongest relationship with SPEI, consistent with evaporative enrichment being jointly constrained by

410 moisture supply and atmospheric demand. Numerous SPEI reconstructions based on $\delta^{18}O_{TRC}$ have also

411 been reported for mid-latitude Europe (An et al., 2023; Freund et al., 2023; Labuhn et al., 2016).

412   Together, these results highlight the potential of $\delta^{18}O_{TRC}$ for hydroclimate reconstructions in the East

413 European Plain. The northern $\delta^{18}O_{TRC}$ chronology exhibits a strong and stable growing-season VPD

414 signal (Fig. 3; Fig. S2; Fig. S6), supporting its use for reconstructing hydroclimate variability at high

415 latitudes. Meanwhile, the significant coherence among chronologies from nearby sites (Fig. 2E), together

416 with the common sensitivity of the three chronologies to regional summer hydroclimate (Fig. 5),

417 underscores the potential of $\delta^{18}O_{TRC}$ for reconstructing regional-scale hydroclimate variability and

418 supports expanding site coverage to improve the spatial representativeness of future reconstructions.

419 **4.3 Compared with TRW, $\delta^{18}O_{TRC}$ provide additional information**

420   Moisture signals in TRW at the northern and central sites are markedly weaker than those in $\delta^{18}O_{TRC}$

421 (Fig. 3; Fig. 6). This contrast is consistent with the growth limitation commonly observed at mid- to high

422 latitudes, where TRW north of approximately 50–60° N is often primarily constrained by summer

423 temperature and is therefore better suited for temperature reconstructions (Dolgova et al., 2022; Solomina

424 and Matskovsky, 2021). By contrast, $\delta^{18}O_{TRC}$ reflects both source-water isotope composition and leaf-

425   water evaporative enrichment, allowing it to retain sensitivity to atmospheric humidity and evaporative

426   demand even when radial growth is not strongly moisture-limited (McCarroll and Loader, 2004; Roden

427   et al., 2000). Thus, in relatively humid, temperature-limited mid- to high-latitude settings, $\delta^{18}O_{TRC}$ may

428   outperform TRW in characterizing hydroclimate variability.

429   At the drier southern site, the strongest correlation between TRW and PDSI is comparable in

430   magnitude to the strongest correlation between $\delta^{18}O_{TRC}$ and SPEI (Fig. 3; Fig. 6). In addition, relative to

431   other humidity metrics, $\delta^{18}O_{TRC}$ shows weaker associations with PDSI in both the original and first-

432   differenced series, whereas TRW mainly reflects PDSI and SM signals (Fig. 6). Because PDSI is widely

433   used to represent drought severity and persistence and is closely related to soil-moisture conditions (Dai

434   et al., 2004), this suggests that under stronger moisture limitation, TRW more directly tracks soil-

435   moisture constraints on radial growth. By contrast, SPEI integrates precipitation supply and potential

436   evapotranspiration and therefore better represents moisture conditions shaped jointly by water supply

437   and atmospheric demand (Vicente-Serrano et al., 2010a). Accordingly, at the drier southern site, TRW

438   tends to preferentially capture soil-moisture variability, whereas $\delta^{18}O_{TRC}$ is more likely to integrate both

439   source-water signals and evaporative enrichment processes.

440   **5 Conclusions**

441   We established three $\delta^{18}O_{TRC}$ chronologies of Scots pine over the East European Plain. We found a

442   clear latitudinal gradient, with lower $\delta^{18}O_{TRC}$ values in the north and higher values in the south. Across

443   sites, $\delta^{18}O_{TRC}$ shows broadly similar response patterns to growing-season and summer climate variables,

444   as well as to $\delta^{18}O_p$, although the dominant controls and response strengths differ among sites. $\delta^{18}O_{TRC}$ at

445   three sites record a coherent signal of regional summer hydroclimate variability, but only the northern

446   chronology exhibits a signal strong and stable enough to support reliable climate reconstruction. In

447   addition, comparison with TRW suggests that $\delta^{18}O_{TRC}$ may be the more suitable hydroclimate proxy in

448   temperature-limited environments, whereas in drier, moisture-limited settings TRW more directly

449   reflects soil-moisture constraints on radial growth, while $\delta^{18}O_{TRC}$ more likely integrates source-water

450   isotopic signals and evaporative enrichment processes. Overall, our study demonstrates that $\delta^{18}O_{TRC}$ is

451   an important proxy for reconstructing the spatiotemporal patterns of hydroclimate variability across the

452   East European Plain.

453

456

457 **Author contributions.** CX, WA, and VM conceived the study. QL performed the data analysis and

458 prepared the original draft with contributions from CX, WA, and RH. CX and TZ acquired funding for

459 this study. OS, VM, and ED collected the samples and provided the tree-ring width data. All authors

460 contributed to the interpretation of the results, critically reviewed and edited the final manuscript, and

461 approved the submitted version.

462

465

468

473

474 **References**

475 Allen, R. G., Pereira, L. S., Raes, D., and Smith, M.: Crop evapotranspiration – Guidelines for computing

476 crop water requirements, FAO Irrigation and Drainage Paper 56, FAO, Rome, 1998.

477 Allison, G. B., Gat, J. R., and Leaney, F. W. J.: The relationship between deuterium and oxygen-18 delta

478 values in leaf water, Chem. Geol. Isot. Geosci. Sect., 58, 145–156, https://doi.org/10.1016/0168-

479 9622(85)90035-1, 1985.

480 Álvarez, C., Christie, D. A., González-Reyes, Á., Veblen, T. T., Helle, G., LeQuesne, C., Rodriguez-

481 Caton, M., Szejner, P., Flores-Sáez, F., Gipoulou-Zúñiga, T., Suazo-Álvarez, M., Muñoz-Salazar, T.,

482 Aliste, D., Morales, M. S., Muñoz, A., and Villalba, R.: Hydroclimate variability in the Tropical Andes

483   recorded by δ18O isotopes from a new network of *Polylepis tarapacana* tree-rings, Glob. Planet. Change,
484   239, 104503, https://doi.org/10.1016/j.gloplacha.2024.104503, 2024.

485   An, W., Xu, C., Marković, S. B., Sun, S., Sun, Y., Gavrilov, M. B., Govedar, Z., Hao, Q., and Guo, Z.:
486   Anthropogenic warming has exacerbated droughts in southern Europe since the 1850s, Commun. Earth
487   Environ., 4, 232, https://doi.org/10.1038/s43247-023-00907-1, 2023.

488   Arosio, T., Leuenberger, M., Nicolussi, K., Esper, J., Krusic, P. J., Bebchuk, T., Tegel, W., Hafner, A.,
489   Kirdyanov, A., Schlüchter, C., Reinig, F., Muschitiello, F., and Büntgen, U.: Tree-ring stable isotopes
490   from the European Alps reveal long-term summer drying over the Holocene, Sci. Adv., 11, eadr4161,
491   https://doi.org/10.1126/sciadv.adr4161, 2025.

492   Balting, D. F., Ionita, M., Wegmann, M., Helle, G., Schleser, G. H., Rimbu, N., Freund, M. B., Heinrich,
493   I., Caldarescu, D., and Lohmann, G.: Large-scale climate signals of a European oxygen isotope network
494   from tree rings, Clim. Past, 17, 1005–1023, https://doi.org/10.5194/cp-17-1005-2021, 2021.

495   Barbour, M. M.: Stable oxygen isotope composition of plant tissue: a review, Funct. Plant Biol., 34, 83–
496   94, https://doi.org/10.1071/FP06228, 2007.

497   Cook, E. R., Solomina, O., Matskovsky, V., Cook, B. I., Agafonov, L., Berdnikova, A., Dolgova, E.,
498   Karpukhin, A., Knysh, N., Kulakova, M., Kuznetsova, V., Kyncl, T., Kyncl, J., Maximova, O.,
499   Panyushkina, I., Seim, A., Tishin, D., Ważny, T., and Yermokhin, M.: The European Russia Drought
500   Atlas (1400–2016 CE), Clim. Dyn., 54, 2317–2335, https://doi.org/10.1007/s00382-019-05115-2, 2020.

501   Dai, A., Trenberth, K. E., and Qian, T.: A Global Dataset of Palmer Drought Severity Index for 1870–
502   2002: Relationship with Soil Moisture and Effects of Surface Warming, J. Hydrometeorol., 5, 1117–
503   1130, https://doi.org/10.1175/JHM-386.1, 2004.

504   Dansgaard, W.: The Abundance of O18 in Atmospheric Water and Water Vapour, Tellus, 5, 461–469,
505   https://doi.org/10.1111/j.2153-3490.1953.tb01076.x, 1953.

506   Dansgaard, W.: Stable isotopes in precipitation, Tellus, 16, 436–468, https://doi.org/10.1111/j.2153-
507   3490.1964.tb00181.x, 1964.

508   Dawson, T. E. and Ehleringer, J. R.: Streamside trees that do not use stream water, Nature, 350, 335–
509   337, https://doi.org/10.1038/350335a0, 1991.

510   De Frenne, P., Zellweger, F., Rodríguez-Sánchez, F., Scheffers, B. R., Hylander, K., Luoto, M., Vellend,
511   M., Verheyen, K., and Lenoir, J.: Global buffering of temperatures under forest canopies, Nat. Ecol.
512   Evol., 3, 744–749, https://doi.org/10.1038/s41559-019-0842-1, 2019.

513   Dolgova, E. A., Solomina, O. N., Matskovsky, V. V., Cherenkova, E. A., and Semenyak, N. S.: Climate
514   signal strength in tree-ring width of spruce growing in the Solovetsky Islands (Russia),
515   Dendrochronologia, 76, 126012, https://doi.org/10.1016/j.dendro.2022.126012, 2022.

516   Field, R. D., Andreu-Hayles, L., D'Arrigo, R. D., Oelkers, R., Luckman, B. H., Morimoto, D., Boucher,
517   E., Gennaretti, F., Hermoso, I., Lavergne, A., and Levesque, M.: Tree-ring cellulose δ18O records similar

518   large-scale climate influences as precipitation δ^{18}O in the Northwest Territories of Canada, Clim. Dyn.,
519   58, 759–776, https://doi.org/10.1007/s00382-021-05932-4, 2022.

520   Freund, M. B., Helle, G., Balting, D. F., Ballis, N., Schleser, G. H., and Cubasch, U.: European tree-ring
521   isotopes indicate unusual recent hydroclimate, Commun. Earth Environ., 4, 26,
522   https://doi.org/10.1038/s43247-022-00648-7, 2023.

523   Gat, J. R.: Oxygen and hydrogen isotopes in the hydrologic cycle, Annu. Rev. Earth Planet. Sci., 24,
524   225–262, https://doi.org/10.1146/annurev.earth.24.1.225, 1996.

525   Harris, I., Osborn, T. J., Jones, P., and Lister, D.: Version 4 of the CRU TS monthly high-resolution
526   gridded multivariate climate dataset, Sci. Data, 7, 109, https://doi.org/10.1038/s41597-020-0453-3, 2020.

527   Haupt, M., Weigl, M., Grabner, M., and Boettger, T.: A 400-year reconstruction of July relative air
528   humidity for the Vienna region (eastern Austria) based on carbon and oxygen stable isotope ratios in
529   tree-ring latewood cellulose of oaks (*Quercus petraea* Matt. Liebl.), Clim. Change, 105, 243–262,
530   https://doi.org/10.1007/s10584-010-9862-1, 2011.

531   Holmes, R. L.: Computer-assisted quality control in tree-ring dating and measurement, Tree-Ring Bull.,
532   43, 69–78, 1983.

533   Huang, R., Xu, C., An, W., Zhao, Q., Zhao, Y., Liu, Y., Grießinger, J., Meier, W. J.-H., and Guo, Z.:
534   Asian continental isoscapes of tree-ring δ^{18}O: implications for paleoclimate and paleoenvironment, Natl.
535   Sci. Rev., 12, nwaf481, https://doi.org/10.1093/nsr/nwaf481, 2025.

536   Hughes, M. K., Olchev, A., Bunn, A. G., Berner, L. T., Losleben, M., and Novenko, E.: Different climate
537   responses of spruce and pine growth in Northern European Russia, Dendrochronologia, 56, 125601,
538   https://doi.org/10.1016/j.dendro.2019.05.005, 2019.

539   Keel, S. G., Joos, F., Spahni, R., Saurer, M., Weigt, R. B., and Klesse, S.: Simulating oxygen isotope
540   ratios in tree ring cellulose using a dynamic global vegetation model, Biogeosciences, 13, 3869–3886,
541   https://doi.org/10.5194/bg-13-3869-2016, 2016.

542   Klimenko, V. and Solomina, O.: Climatic Variations in the East European Plain During the Last
543   Millennium: State of the Art, in: The Polish Climate in the European Context: An Historical Overview,
544   edited by: Przybylak, R., Springer Netherlands, Dordrecht, 71–101, https://doi.org/10.1007/978-90-481-
545   3167-9_3, 2010.

546   Krklec, K., Domínguez-Villar, D., and Lojen, S.: The impact of moisture sources on the oxygen isotope
547   composition of precipitation at a continental site in central Europe, J. Hydrol., 561, 810–821,
548   https://doi.org/10.1016/j.jhydrol.2018.04.045, 2018.

549   Kuznetsova, V. V. and Solomina, O. N.: Contrasting climate signals across a Scots pine (*Pinus sylvestris*
550   L.) tree-ring network in the Middle Volga (European Russia), Dendrochronologia, 73, 125957,
551   https://doi.org/10.1016/j.dendro.2022.125957, 2022.

552   Labuhn, I., Daux, V., Girardclos, O., Stievenard, M., Pierre, M., and Masson-Delmotte, V.: French

553 summer droughts since 1326 CE: a reconstruction based on tree ring cellulose $\delta^{18}O$, Clim. Past, 12, 1101–
554 1117, https://doi.org/10.5194/cp-12-1101-2016, 2016.

555 Lange, J., Buras, A., Cruz-García, R., Gurskaya, M., Jalkanen, R., Kukarskih, V., Seo, J.-W., and
556 Wilmking, M.: Climate Regimes Override Micro-Site Effects on the Summer Temperature Signal of
557 Scots Pine at Its Northern Distribution Limits, Front. Plant Sci., 9, 1597,
558 https://doi.org/10.3389/fpls.2018.01597, 2018.

559 Langebroek, P. M., Werner, M., and Lohmann, G.: Climate information imprinted in oxygen-isotopic
560 composition of precipitation in Europe, Earth Planet. Sci. Lett., 311, 144–154,
561 https://doi.org/10.1016/j.epsl.2011.08.049, 2011.

562 Leland, C., Andreu-Hayles, L., Cook, E. R., Anchukaitis, K. J., Byambasuren, O., Davi, N., Hessl, A.,
563 Martin-Benito, D., Nachin, B., and Pederson, N.: Impacts of climate and tree morphology on tree-ring
564 stable isotopes in central Mongolia, Tree Physiol., 43, 539–555,
565 https://doi.org/10.1093/treephys/tpac142, 2023.

566 Liu, Y., Wang, L., Zhou, W., and Chen, W.: Three Eurasian teleconnection patterns: spatial structures,
567 temporal variability, and associated winter climate anomalies, Clim. Dyn., 42, 2817–2839,
568 https://doi.org/10.1007/s00382-014-2163-z, 2014.

569 Loader, N. J., Robertson, I., Barker, A. C., Switsur, V. R., and Waterhouse, J. S.: An improved technique
570 for the batch processing of small wholewood samples to α-cellulose, Chem. Geol., 136, 313–317,
571 https://doi.org/10.1016/S0009-2541(96)00133-7, 1997.

572 Matskovsky, V.: Climatic signal in tree-ring width chronologies of conifers in European Russia, Int. J.
573 Climatol., 36, 3398–3406, https://doi.org/10.1002/joc.4563, 2016.

574 Matskovsky, V., Dolgova, E., Lomakin, N., and Matveev, S.: Dendroclimatology and historical
575 climatology of Voronezh region, European Russia, since 1790s, Int. J. Climatol., 37, 3057–3066,
576 https://doi.org/10.1002/joc.4896, 2017.

577 Matskovsky, V. V., Kuznetsova, V. V., Semenyak, N. S., Turchinskaya, S. M., Zazovskaya, E. P.,
578 Engovatova, A. V., Lazarev, A. S., Zhdanova, E. Yu., Dolgova, E. A., and Solomina, O. N.:
579 Dendroclimatic potential of stable carbon isotopes in tree-ring cellulose of *Pinus sylvestris* L. in the
580 Yaroslavl and Kostroma regions [in Russian], Geomorfologiya i Paleogeografiya, 53, 74–82,
581 https://doi.org/10.31857/S0435428122030099, 2022.

582 Matulewski, P., Buchwal, A., and Makohonienko, M.: Higher climatic sensitivity of Scots pine (*Pinus
583 sylvestris* L.) subjected to tourist pressure on a hiking trail in the Brodnica Lakeland, NE Poland,
584 Dendrochronologia, 54, 78–86, https://doi.org/10.1016/j.dendro.2019.02.008, 2019.

585 Matveev, S., Tishin, D., Maximchuk, P., and Zhuravleva, I.: Seasonal radial growth dynamics of Scots
586 pine (*Pinus silvestris* L.) in Voronezh region (Russia), IOP Conf. Ser. Earth Environ. Sci., 595, 012044,
587 https://doi.org/10.1088/1755-1315/595/1/012044, 2020.

588 Matveev, S. M., Chendev, Yu. G., Lupo, A. R., Hubbart, J. A., and Timashchuk, D. A.: Climatic Changes

589   in the East-European Forest-Steppe and Effects on Scots Pine Productivity, Pure Appl. Geophys., 174,
590   427–443, https://doi.org/10.1007/s00024-016-1420-y, 2017.

591   McCarroll, D. and Loader, N. J.: Stable isotopes in tree rings, Quat. Sci. Rev., 23, 771–801,
592   https://doi.org/10.1016/j.quascirev.2003.06.017, 2004.

593   McNally, A., Arsenault, K., Kumar, S., Shukla, S., Peterson, P., Wang, S., Funk, C., Peters-Lidard, C.
594   D., and Verdin, J. P.: A land data assimilation system for sub-Saharan Africa food and water security
595   applications, Sci. Data, 4, 170012, https://doi.org/10.1038/sdata.2017.12, 2017.

596   Moberg, A., Jones, P. D., Lister, D., Walther, A., Brunet, M., Jacobeit, J., Alexander, L. V., Della-Marta,
597   P. M., Luterbacher, J., Yiou, P., Chen, D., Klein Tank, A. M. G., Saladié, O., Sigró, J., Aguilar, E.,
598   Alexandersson, H., Almarza, C., Auer, I., Barriendos, M., Begert, M., Bergström, H., Böhm, R., Butler,
599   C. J., Caesar, J., Drebs, A., Founda, D., Gerstengarbe, F., Micela, G., Maugeri, M., Österle, H., Pandzic,
600   K., Petrakis, M., Srnec, L., Tolasz, R., Tuomenvirta, H., Werner, P. C., Linderholm, H., Philipp, A.,
601   Wanner, H., and Xoplaki, E.: Indices for daily temperature and precipitation extremes in Europe analyzed
602   for   the   period   1901–2000,   J.   Geophys.   Res.-Atmos.,   111,   D22106,
603   https://doi.org/10.1029/2006JD007103, 2006.

604   Morozova, S. V., Denisov, K. E., Polyanskaya, E. A., Kondakov, K. S., Korotkova, N. V., and Gafurov,
605   R. R.: Changes in the Atmospheric Circulation Regime in the Context of Global Climate Trends in the
606   Atlantic-Eurasian Sector of the Northern Hemisphere, Geogr. Nat. Resour., 44, 191–197,
607   https://doi.org/10.1134/S1875372823030083, 2023.

608   Mutlu, H., Köse, N., Akkemik, Ü., Aral, D., Kaya, A., Manning, S. W., Pearson, C. L., and Dalfes, N.:
609   Environmental and climatic signals from stable isotopes in Anatolian tree rings, Turkey, Reg. Environ.
610   Change, 12, 559–570, https://doi.org/10.1007/s10113-011-0273-2, 2012.

611   Nagavciuc, V., Michel, S. L. L., Balting, D. F., Helle, G., Freund, M., Schleser, G. H., Steger, D. N.,
612   Lohmann, G., and Ionita, M.: A past and present perspective on the European summer vapor pressure
613   deficit, Clim. Past, 20, 573–595, https://doi.org/10.5194/cp-20-573-2024, 2024.

614   Panyushkina, I. P., Karpukhin, A. A., and Engovatova, A. V.: Moisture record of the Upper Volga
615   catchment between AD 1430 and 1600 supported by a δ^{13}C tree-ring chronology of archaeological pine
616   timbers, Dendrochronologia, 39, 24–31, https://doi.org/10.1016/j.dendro.2016.02.002, 2016.

617   Rinne, K.: 400-year May-August Precipitation Reconstruction for England Using Stable Oxygen Isotope
618   Ratios (δ^{18}O) of Tree Rings, Quat. Int., 279–280, 403–404, https://doi.org/10.1016/j.quaint.2012.08.1281,
619   2012.

620   Roden, J. S., Lin, G., and Ehleringer, J. R.: A mechanistic model for interpretation of hydrogen and
621   oxygen isotope ratios in tree-ring cellulose, Geochim. Cosmochim. Acta, 64, 21–35,
622   https://doi.org/10.1016/S0016-7037(99)00195-7, 2000.

623   Römer, P., Wieland, A., Torbenson, M. C. A., Reinig, F., Ziaco, E., Frigo, D., Greule, M., Urban, O.,
624   Čáslavský, J., Pernicová, N., Trnka, M., Carrer, M., Büntgen, U., Keppler, F., and Esper, J.: Covariance
625   and climate signals among state-of-the-art tree-ring proxies, Quat. Sci. Rev., 355, 109270,

626   https://doi.org/10.1016/j.quascirev.2025.109270, 2025.

627   Rozanski, K., Araguás-Araguás, L., and Gonfiantini, R.: Relation Between Long-Term Trends of
628   Oxygen-18 Isotope Composition of Precipitation and Climate, Science, 258, 981–985,
629   https://doi.org/10.1126/science.258.5084.981, 1992.

630   Saurer, M., Cherubini, P., and Siegwolf, R.: Oxygen isotopes in tree rings of *Abies alba*: The climatic
631   significance of interdecadal variations, J. Geophys. Res.-Atmos., 105, 12461–12470,
632   https://doi.org/10.1029/2000JD900160, 2000.

633   Semenyak, N. and Dolgova, E.: Dendroclimatic signals in the pine and spruce chronologies in the
634   Solovetsky Archipelago, Dendrochronologia, 77, 126029, https://doi.org/10.1016/j.dendro.2022.126029,
635   2023.

636   Solomina, O. and Matskovsky, V.: Dendrochronology in European Russia in the Early 21st Century:
637   State of the Art, Front. Ecol. Evol., 9, 738199, https://doi.org/10.3389/fevo.2021.738199, 2021.

638   Spinoni, J., Naumann, G., Vogt, J., and Barbosa, P.: European drought climatologies and trends based
639   on a multi-indicator approach, Glob. Planet. Change, 127, 50–57,
640   https://doi.org/10.1016/j.gloplacha.2015.01.012, 2015.

641   Sternberg, L. and Ellsworth, P. F. V.: Divergent Biochemical Fractionation, Not Convergent
642   Temperature, Explains Cellulose Oxygen Isotope Enrichment across Latitudes, PLoS ONE, 6, e28040,
643   https://doi.org/10.1371/journal.pone.0028040, 2011.

644   Tishin, D. V., Chizhikova, N. A., Zhuravleva, I. V., and Chugunov, R. G.: Xylogenesis of Pinus sylvestris
645   L. growing in the northern island ecosystems [in Russian], Lesotekhnicheskii Zhurnal (Forestry
646   Engineering Journal), 6, 89–97, https://doi.org/10.12737/23439, 2016.

647   Treydte, K., Frank, D., Esper, J., Andreu, L., Bednarz, Z., Berninger, F., Boettger, T., D'Alessandro, C.
648   M., Etien, N., Filot, M., Grabner, M., Guillemin, M. T., Gutierrez, E., Haupt, M., Helle, G., Hilasvuori,
649   E., Jungner, H., Kalela-Brundin, M., Krapiec, M., Leuenberger, M., Loader, N. J., Masson-Delmotte, V.,
650   Pazdur, A., Pawelczyk, S., Pierre, M., Planells, O., Pukiene, R., Reynolds-Henne, C. E., Rinne, K. T.,
651   Saracino, A., Saurer, M., Sonninen, E., Stievenard, M., Switsur, V. R., Szczepanek, M., Szychowska-
652   Krapiec, E., Todaro, L., Waterhouse, J. S., Weigl, M., and Schleser, G. H.: Signal strength and climate
653   calibration of a European tree-ring isotope network, Geophys. Res. Lett., 34, L24302,
654   https://doi.org/10.1029/2007GL031106, 2007.

655   Treydte, K., Liu, L., Padrón, R. S., Martínez-Sancho, E., Babst, F., Frank, D. C., Gessler, A., Kahmen,
656   A., Poulter, B., Seneviratne, S. I., Stegehuis, A. I., Wilson, R., Andreu-Hayles, L., Bale, R., Bednarz, Z.,
657   Boettger, T., Berninger, F., Büntgen, U., Daux, V., Dorado-Liñán, I., Esper, J., Friedrich, M., Gagen, M.,
658   Grabner, M., Grudd, H., Gunnarsson, B. E., Gutiérrez, E., Hafner, P., Haupt, M., Hilasvuori, E., Heinrich,
659   I., Helle, G., Jalkanen, R., Jungner, H., Kalela-Brundin, M., Kessler, A., Kirchhefer, A., Klesse, S.,
660   Krapiec, M., Levanič, T., Leuenberger, M., Linderholm, H. W., McCarroll, D., Masson-Delmotte, V.,
661   Pawelczyk, S., Pazdur, A., Planells, O., Pukiene, R., Rinne-Garmston, K. T., Robertson, I., Saracino, A.,
662   Saurer, M., Schleser, G. H., Seftigen, K., Siegwolf, R. T. W., Sonninen, E., Stievenard, M., Szychowska-

663 Krapiec, E., Szymaszek, M., Todaro, L., Waterhouse, J. S., Weigl-Kuska, M., Weigt, R. B., Wimmer, R.,
664 Woodley, E. J., Vitas, A., Young, G., and Loader, N. J.: Recent human-induced atmospheric drying
665 across Europe unprecedented in the last 400 years, Nat. Geosci., 17, 58–65,
666 https://doi.org/10.1038/s41561-023-01335-8, 2024.

667 Trouet, V. and Van Oldenborgh, G. J.: KNMI Climate Explorer: A Web-Based Research Tool for High-
668 Resolution Paleoclimatology, Tree-Ring Res., 69, 3–13, https://doi.org/10.3959/1536-1098-69.1.3, 2013.

669 Vicente-Serrano, S. M., Beguería, S., and López-Moreno, J. I.: A Multiscalar Drought Index Sensitive
670 to Global Warming: The Standardized Precipitation Evapotranspiration Index, J. Clim., 23, 1696–1718,
671 https://doi.org/10.1175/2009JCLI2909.1, 2010a.

672 Vicente-Serrano, S. M., Beguería, S., López-Moreno, J. I., Angulo, M., and El Kenawy, A.: A New
673 Global 0.5° Gridded Dataset (1901–2006) of a Multiscalar Drought Index: Comparison with Current
674 Drought Index Datasets Based on the Palmer Drought Severity Index, J. Hydrometeorol., 11, 1033–1043,
675 https://doi.org/10.1175/2010JHM1224.1, 2010b.

676 Wang, W., Zeng, X., Liu, X., An, W., and Zhang, L.: Temporal evolution of the influence of atmospheric
677 circulation on regional cloud cover as revealed by tree-ring $\delta^{18}O$ in southwestern China, Glob. Planet.
678 Change, 208, 103690, https://doi.org/10.1016/j.gloplacha.2021.103690, 2022.

679 Werner, M., Langebroek, P. M., Carlsen, T., Herold, M., and Lohmann, G.: Stable water isotopes in the
680 ECHAM5 general circulation model: Toward high-resolution isotope modeling on a global scale, J.
681 Geophys. Res., 116, D15109, https://doi.org/10.1029/2011JD015681, 2011.

682 Wigley, T. M. L., Briffa, K. R., and Jones, P. D.: On the Average Value of Correlated Time Series, with
683 Applications in Dendroclimatology and Hydrometeorology, J. Clim. Appl. Meteorol., 23, 201–213,
684 https://doi.org/10.1175/1520-0450(1984)023%253C0201:OTAVOC%253E2.0.CO;2, 1984.

685 Xu, C., Sano, M., and Nakatsuka, T.: Tree ring cellulose $\delta^{18}O$ of *Fokienia hodginsii* in northern Laos: A
686 promising proxy to reconstruct ENSO?, J. Geophys. Res.-Atmos., 116, D24109,
687 https://doi.org/10.1029/2011JD016694, 2011.

688 Xu, C., Sano, M., and Nakatsuka, T.: A 400-year record of hydroclimate variability and local ENSO
689 history in northern Southeast Asia inferred from tree-ring $\delta^{18}O$, Palaeogeogr. Palaeoclimatol. Palaeoecol.,
690 386, 588–598, https://doi.org/10.1016/j.palaeo.2013.06.025, 2013a.

691 Xu, C., Zheng, H., Nakatsuka, T., and Sano, M.: Oxygen isotope signatures preserved in tree ring
692 cellulose as a proxy for April–September precipitation in Fujian, the subtropical region of southeast
693 China, J. Geophys. Res.-Atmos., 118, 12805–12815, https://doi.org/10.1002/2013JD019803, 2013b.

694 Xu, C., Zhao, Q., An, W., Wang, S., Tan, N., Sano, M., Nakatsuka, T., Borhara, K., and Guo, Z.: Tree-
695 ring oxygen isotope across monsoon Asia: Common signal and local influence, Quat. Sci. Rev., 269,
696 107156, https://doi.org/10.1016/j.quascirev.2021.107156, 2021.

697 Xu, C., Wang, S.-Y. S., Borhara, K., Buckley, B., Tan, N., Zhao, Y., An, W., Sano, M., Nakatsuka, T.,
698 and Guo, Z.: Asian-Australian summer monsoons linkage to ENSO strengthened by global warming, npj

699   Clim. Atmos. Sci., 6, 8, https://doi.org/10.1038/s41612-023-00341-2, 2023.

700   Xu, C., Huang, R., An, W., Zhao, Q., Zhao, Y., Ren, J., Liu, Y., and Guo, Z.: Tree ring oxygen isotope
701   in Asia, Glob. Planet. Change, 232, 104348, https://doi.org/10.1016/j.gloplacha.2023.104348, 2024.

702   Zellweger, F., De Frenne, P., Lenoir, J., Vangansbeke, P., Verheyen, K., Bernhardt-Römermann, M.,
703   Baeten, L., Hédl, R., Berki, I., Brunet, J., Van Calster, H., Chudomelová, M., Decocq, G., Dirnböck, T.,
704   Durak, T., Heinken, T., Jaroszewicz, B., Kopecký, M., Máliš, F., Macek, M., Malicki, M., Naaf, T.,
705   Nagel, T. A., Ortmann-Ajkai, A., Petřík, P., Pielech, R., Reczyńska, K., Schmidt, W., Standovár, T.,
706   Świerkosz, K., Teleki, B., Vild, O., Wulf, M., and Coomes, D.: Forest microclimate dynamics drive plant
707   responses to warming, Science, 368, 772–775, https://doi.org/10.1126/science.aba6880, 2020.

708   Zharkov, M. S., Fonti, M. V., Trushkina, T. V., Barinov, V. V., Taynik, A. V., Porter, T. J., Saurer, M.,
709   and Churakova (Sidorova), O. V.: Mixed Temperature-Moisture Signal in $\delta^{18}O$ Records of Boreal
710   Conifers from the Permafrost Zone, Atmosphere, 12, 1416, https://doi.org/10.3390/atmos12111416,
711   2021.

712   Zolina, O., Simmer, C., Belyaev, K., Kapala, A., and Gulev, S.: Improving Estimates of Heavy and
713   Extreme Precipitation Using Daily Records from European Rain Gauges, J. Hydrometeorol., 10, 701–
714   716, https://doi.org/10.1175/2008JHM1055.1, 2009.

715